Gold nanorods for intravital vascular imaging of preneoplastic oral mucosa

Saam Motamedi,[1] Tuya Shilagard,[1] Kert Edward,[1] Luke Koong,[1,2] Suimin Qui,[3,4] and Gracie Vargas[1,4,5,*]

[1]*Center for Biomedical Engineering, The University of Texas Medical Branch, Galveston, TX 77555-0456*
[2]*Present address, Department of Biochemistry and Molecular Biology, The University of Texas Medical Branch, Galveston, TX 77555*
[3]*Department of Pathology, The University of Texas Medical Branch, Galveston, TX 77555-0456*
[4]*Center for Cancers of the Head and Neck, The University of Texas Medical Branch, Galveston, TX 77555-04565*
[5]*Department of Neuroscience & Cell Biology, The University of Texas Medical Branch, Galveston, TX 77555-0456*
**grvargas@utmb.edu*

Abstract: We explore the feasibility of using gold nanorods with efficient two-photon luminescence properties as contrast agents for intravital imaging of neoplasia. This investigation spanned *ex vivo* characterization in cells/tissue to *in vivo* implementation in an oral carcinogenesis model. GNRs were >40 times brighter than surrounding tissue. Intravital imaging revealed 3D microvasculature, and in dysplasia, abnormal vessels (dense and tortuous) compared to normal. GNRs were diffusely distributed in lesions after 24 hours. No known previous study has revealed abnormal vessel structure in dysplasia by imaging. Results suggest GNRs can function as high-contrast agents for *in vivo* visualization of carcinogenesis features.

OCIS codes: (180.4315) Nonlinear microscopy; (170.3880) Medical and biological imaging; (160.4236) Nanomaterials.

References and links

1. X. Huang, I. H. El-Sayed, and M. A. El-Sayed, "Applications of gold nanorods for cancer imaging and photothermal therapy," Methods Mol. Biol. **624**, 343–357 (2010).
2. J. Park, A. Estrada, K. Sharp, K. Sang, J. A. Schwartz, D. K. Smith, C. Coleman, J. D. Payne, B. A. Korgel, A. K. Dunn, and J. W. Tunnell, "Two-photon-induced photoluminescence imaging of tumors using near-infrared excited gold nanoshells," Opt. Express **16**(3), 1590–1599 (2008).
3. H. Wang, T. B. Huff, D. A. Zweifel, W. He, P. S. Low, A. Wei, and J. X. Cheng, "In vitro and in vivo two-photon luminescence imaging of single gold nanorods," Proc. Natl. Acad. Sci. U.S.A. **102**(44), 15752–15756 (2005).
4. N. J. Durr, T. Larson, D. K. Smith, B. A. Korgel, K. Sokolov, and A. Ben-Yakar, "Two-photon luminescence imaging of cancer cells using molecularly targeted gold nanorods," Nano Lett. **7**(4), 941–945 (2007).
5. I. H. El-Sayed, X. H. Huang, and M. A. El-Sayed, "Selective laser photo-thermal therapy of epithelial carcinoma using anti-EGFR antibody conjugated gold nanoparticles," Cancer Lett. **239**(1), 129–135 (2006).
6. M. Eghtedari, A. V. Liopo, J. A. Copland, A. A. Oraevsky, and M. Motamedi, "Engineering of hetero-functional gold nanorods for the in vivo molecular targeting of breast cancer cells," Nano Lett. **9**(1), 287–291 (2009).
7. S. E. Gratton, P. A. Ropp, P. D. Pohlhaus, J. C. Luft, V. J. Madden, M. E. Napier, and J. M. DeSimone, "The effect of particle design on cellular internalization pathways," Proc. Natl. Acad. Sci. U.S.A. **105**(33), 11613–11618 (2008).
8. X. Qu, J. Wang, Z. Zhang, N. Koop, R. Rahmanzadeh, and G. Hüttmann, "Imaging of cancer cells by multiphoton microscopy using gold nanoparticles and fluorescent dyes," J. Biomed. Opt. **13**(3), 031217 (2008).
9. L. Tong, W. He, Y. Zhang, W. Zheng, and J. X. Cheng, "Visualizing systemic clearance and cellular level biodistribution of gold nanorods by intrinsic two-photon luminescence," Langmuir **25**(21), 12454–12459 (2009).
10. American Cancer Society, *Cancer Facts & Figures 2002* (American Cancer Society, New York, 2002).
11. S. Silverman, *Oral Cancer*, 3rd ed. (The American Cancer Society, Atlanta, 1990).
12. S. A. Liu, Y. K. Wong, J. C. Lin, C. K. Poon, K. C. Tung, and W. C. Tsai, "Impact of recurrence interval on survival of oral cavity squamous cell carcinoma patients after local relapse," Otolaryngol. Head Neck Surg. **136**(1), 112–118 (2007).
13. R. Weissleder and M. J. Pittet, "Imaging in the era of molecular oncology," Nature **452**(7187), 580–589 (2008).
14. J. Sun, T. Shilagard, B. Bell, M. Motamedi, and G. Vargas, "In vivo multimodal nonlinear optical imaging of mucosal tissue," Opt. Express **12**(11), 2478–2486 (2004).

#140464 - $15.00 USD Received 4 Jan 2011; revised 8 Apr 2011; accepted 11 Apr 2011; published 13 Apr 2011

15. J. Paoli, M. Smedh, and M. B. Ericson, "Multiphoton laser scanning microscopy--a novel diagnostic method for superficial skin cancers," Semin. Cutan. Med. Surg. **28**(3), 190–195 (2009).
16. P. Wilder-Smith, K. Osann, N. Hanna, N. El Abbadi, M. Brenner, D. Messadi, and T. Krasieva, "In vivo multiphoton fluorescence imaging: a novel approach to oral malignancy," Lasers Surg. Med. **35**(2), 96–103 (2004).
17. M. C. Skala, J. M. Squirrell, K. M. Vrotsos, J. C. Eickhoff, A. Gendron-Fitzpatrick, K. W. Eliceiri, and N. Ramanujam, "Multiphoton microscopy of endogenous fluorescence differentiates normal, precancerous, and cancerous squamous epithelial tissues," Cancer Res. **65**(4), 1180–1186 (2005).
18. G. Vargas, T. Shilagard, J. Sun, and M. Motamedi, "In vivo multiphoton and second harmonic generation microscopy of epithelial carcinogenesis," *Proc. SPIE* **6091**, 000–000 (2006).
19. M. C. Skala, K. M. Riching, A. Gendron-Fitzpatrick, J. Eickhoff, K. W. Eliceiri, J. G. White, and N. Ramanujam, "In vivo multiphoton microscopy of NADH and FAD redox states, fluorescence lifetimes, and cellular morphology in precancerous epithelia," Proc. Natl. Acad. Sci. U.S.A. **104**(49), 19494–19499 (2007).
20. G. Vargas, T. Shilagard, K. H. Ho, and S. McCammon, "Multiphoton autofluorescence microscopy and second harmonic generation microscopy of oral epithelial neoplasms," Conf. Proc. IEEE Eng. Med. Biol. Soc. **2009**, 6311–6313 (2009).
21. V. A. Resto, M. M. Burdick, N. M. Dagia, S. D. McCammon, S. M. Fennewald, and R. Sackstein, "L-selectin-mediated lymphocyte-cancer cell interactions under low fluid shear conditions," J. Biol. Chem. **283**(23), 15816–15824 (2008).
22. G. Shklar, "Experimental pathology of oral cancer," in *Oral Cancer*, G. Shklar, ed. (W.B. Sanders, 1984), pp. 41–54.
23. A. Ebihara, T. B. Krasieva, L.-H. Liaw, S. Fago, D. Messadi, K. Osann, and P. Wilder-Smith, "Detection and diagnosis of oral cancer by light-induced fluorescence," Lasers Surg. Med. **32**(1), 17–24 (2003).
24. A. M. Kluftinger, N. L. Davis, N. F. Quenville, S. Lam, J. Hung, and B. Palcic, "Detection of squamous cell cancer and pre-cancerous lesions by imaging of tissue autofluorescence in the hamster cheek pouch model," Surg. Oncol. **1**(2), 183–188 (1992).
25. V. L. Noonan and S. Kabani, "Diagnosis and management of suspicious lesions of the oral cavity," Otolaryngol. Clin. North Am. **38**(1), 21–35, vii (2005) (vii.).
26. F. Nussenbaum and I. M. Herman, "Tumor angigoenesis: insights and inovations," J. Oncolog. **2010**, 132641 (2010).
27. N. Mohtasham, S. Babakoohi, J. Salehinejad, L. Montaser-Kouhsari, M. T. Shakeri, S. Shojaee, N. S. Sistani, and A. Firooz, "Mast cell density and angiogenesis in oral dysplastic epithelium and low- and high-grade oral squamous cell carcinoma," Acta Odontol. Scand. **68**(5), 300–304 (2010).
28. E. Z. Michailidou, A. K. Markopoulos, and D. Z. Antoniades, "Mast cells and angiogenesis in oral malignant and premalignant lesions," Open Dent. J. **2**(1), 126–132 (2008).
29. M. Raica, A. M. Cimpean, and D. Ribatti, "Angiogenesis in pre-malignant conditions," Eur. J. Cancer **45**(11), 1924–1934 (2009).

1. Introduction

Highly efficient nanoparticles exhibiting two-photon induced photoluminescence are of great interest as contrast agents for *in vivo* optical imaging, including molecular imaging of cancer, due to their ability to be excited with extremely low incident powers, their well-defined spectral properties, and their potential for enabling large imaging depths using intravital two-photon microscopy [1,2]. Gold nanorods (GNRs) exhibit very bright two-photon luminescence (TPL) signals that have been shown to be many times brighter than traditional fluorophores, such as rhodamine or native fluorophores [3,4]. GNRs can also be bioconjugated to enable molecular targeting [4–6]. Additionally, gold is considered a relatively biocompatible material compared to other nanoparticle materials, and has promising applications in preclinical *in vivo* imaging [6,7]. Previous studies demonstrating the potential benefits of GNRs as high contrast TPL agents for cancer imaging have been reported for studies performed in cell cultures or tissue phantoms [4,8]. One known study has imaged GNRs *in vivo* for clearance and biodistribution characterization in mice [9]. Gold nanoshells have been imaged *in vivo* and though one study found their properties to be comparable to GNRs, only nanoshells were delivered *in vivo* [2]. No known reports have demonstrated the potential use of GNRs as contrast agents for intravital multi-photon imaging in neoplasia.

Epithelial neoplasms account for the majority of cancers, and although they occur at epithelial surfaces, they can span several hundred microns in depth. One of the primary challenges for treating cancer is early detection. In fact, the probability for cancer survival is significantly correlated with its stage of development at diagnosis. For example, in the case of

#140464 - $15.00 USD Received 4 Jan 2011; revised 8 Apr 2011; accepted 11 Apr 2011; published 13 Apr 2011

oral cancer, which is associated with a 5-year survival rate of 55%, patients with a localized malignancy have a survival rate of 82%, compared to a survival rate of 46% in patients where the disease has spread to adjoining areas, and 21% after metastasis [10,11]. Thus, it is thought that one of the most effective ways to battle cancer is through early detection, before it metastasizes, when it is still possible to successfully treat local occurrence with conventional techniques such as chemotherapy or surgical removal. Furthermore, oral cancer is associated with a high recurrence rate which has a higher morbidity and mortality than primary occurrence, necessitating early detection of recurrence as well as margin identification [12]. There is a clear need for the development of robust and sensitive detection methods for identifying high risk premalignant (e.g. dysplasia) and malignant regions during early stages of neoplastic transformation. In recent years, there has been a growing recognition for the need to develop new imaging techniques that can be combined with efficient contrast agents, including molecular-specific agents, to reveal early neoplastic changes [13]. Such capabilities would be highly beneficial for the enhanced understanding of the multi-step process of epithelial carcinogenesis, toward assessment of candidate therapies, and toward developing effective early diagnostic approaches. Two-photon microscopy is a particularly attractive possibility as imaging depths are sufficient to image both epithelium and stromal components of oral mucosal tissue [14,15]. Although two-photon microscopy has been explored for *in vivo* imaging of oral squamous cell carcinoma (SCC), image contrast in previous studies has thus far primarily been provided by autofluorescence (AF) [16–20].

GNRs as TPL contrast agents could be highly useful for delineating areas of abnormality versus surrounding normal tissue in oral carcinogenesis. In this study, we present two-photon induced luminescence imaging of nontargeted GNRs in an *in vivo* animal model for oral carcinogenesis. Potential benefits of the gold nanorods are explored for providing contrast to visualize subsurface details of abnormal vasculature in precancerous lesions (dysplasia) using very low incident powers where autofluorescent background is not detected. Quantitative image parameters describing vessel properties are qualitatively correlated to histology observations.

2. Materials and methods

2.1. Two photon microscopy system

Two-photon microscopy was performed on a custom-built system based on a modification of a Zeiss Confocal LSM 410 microscope and outfitted with optics designed for ultrafast laser excitation and nondescanned detection of multiphoton emission [14]. The excitation source was a femtosecond Ti:sapphire laser (Tsunami, Spectra Physics/Newport, Irvine CA) having a 5W frequency-doubled Nd:YVO pump laser. The system operated with a typical pulse width of 140 fs prior to the objective (40x 0.8 N.A. water). An epi-configuration was used for collection of emitted light and detected using a cooled PMT placed in a nondescanned configuration (R6060, Hamamatsu, Japan). Emission was collected in the range of 450-650 nm. Imaging field of view was 320 x 320 μm and a z-interval of 1 μm was used for acquiring zstacks. Image reconstructions of two-photon micrograph stacks were performed using Imaris 3D visualization software (Bitplane Inc., St. Paul, MN). Confocal reflectance microscopy in the case of surface tissue imaging to demonstrate surface features of areas imaged by TPL was accomplished using the same microscope and objective in confocal mode, operating at an illumination wavelength of 568 nm from an Ar:Kr ion laser. Reflected light in confocal reflectance microscopy was collected using a cooled PMT (R6060, Hamamatsu, Japan) along the descanned confocal path.

Spectral profiles of GNRs were obtained using a microspectroscopy unit adapted to the detection port of the two-photon microscope. The unit consisted of a 300 g/mm grating spectrograph (SpectraPro-150, Princeton Instruments) and a computer-controlled electron multiplying CCD camera (Newton DU970N, Andor Technology) mounted to the exit port of

#140464 - $15.00 USD Received 4 Jan 2011; revised 8 Apr 2011; accepted 11 Apr 2011; published 13 Apr 2011

the spectrograph. Calibration of the system was performed using a mercury-argon light source and the final spectra were corrected for the optical transmission characteristics of the microscope. The spectral window of the spectroscope ranged from approximately 200 nm to 700 nm with a resolution of 0.1 nm per pixel. A lateral displacement mirror angled at 45° was used to direct the TPL signal to either the spectrograph for spectroscopy or photomultiplier for imaging.

2.2. Gold nanorods

Commercially available GNRs were used for these studies (Nanopartz Inc., Loveland CO). GNRs were 10x38 nm in dimension and had a longitudinal surface plasmon resonance (LSPR) peak at 780 nm and a transverse surface plasmon resonance (TSPR) peak at 512 nm.

2.3. Cells and animal model

In this study, we first characterized the GNRs in cells to establish expected image parameters in tissues and in the *in vivo* oral precancer/cancer model. Oral squamous cell carcinoma cells (JHU-19) were seeded onto poly-D-lysine coated imaging dishes having a #1.5 coverslip bottom (Matek Corporation, Ashland, MA) and allowed to reach confluence [21]. Cells were then incubated with methyl-terminated Ntherapy GNRs (Nanopartz Inc., Loveland, CO). For incubation, 20 µl of 100 nM Ntherapy GNR stock (optical density 50) was added to 2 ml Dulbecco's Modified Eagle Medium (DMEM) without phenol red for time periods ranging from 10 minutes to 24 hours. The 2 hour time point was found to be acceptable due to high uptake of the GNRs and thus, in subsequent imaging, a 2 hour incubation time was used. Prior to imaging, cells were viewed under bright field microscopy to visualize morphology of cells and attachment to the imaging dish. Samples were rinsed with PBS to remove excess GNRs. Unlabeled cultures underwent the same procedures except for the delivery of GNRs. Two-photon microscopy imaging of labeled and unlabeled cells was performed using a range of incident powers from 0.2 mW to >6 mW and incident power versus emission signal plots were created.

Animal studies were performed in a hamster model for oral precancers and cancer. Oral carcinogenesis was induced in the buccal pouch of Golden Syrian hamsters by thrice-weekly topical application of 0.5% 9,10-dimethyl-1,2-benzanthracene (DMBA). This is a widely accepted model that closely mimics the stages of precancers and oral squamous cell carcinoma in humans both in histology and in the expression of key molecular biomarkers [22–24]. Hamsters received DMBA treatment for 12 weeks, after which a variety of preneoplastic and neoplastic lesions were present throughout the buccal mucosa.

2.4. Ex vivo imaging

For *ex vivo* studies, hamsters were first anesthetized using a mixture of Ketamine (100mg/kg)/Xylazine (10mg/kg) mixture given i.p. The buccal pouch was everted and secured to a flat sample holder which interfaced onto the microscope stage for imaging. The anesthetized hamster was held in a supine position to access the sublingual surface where the sublingual veins (*V. sublingualis*) run from basis to the apex of the tongue. An intravenous (i.v.) injection of GNRs (0.2 cc of 100 nM (50 optical density) (Ntrackers, Nanopartz)) into the sublingual vein was given using a 26 gauge needle and the time of injection was noted The hamster was then placed on the imaging stage, and two-photon imaging commenced 10 minutes following the noted time of injection, targeting the microvasculature in the *in vivo* buccal pouch to confirm the successful delivery of the GNRs into the vascular space. Visible lesions having the appearance of leukoplakia or early tumor masses were biopsied 24 hours post injection. Leukoplakia are clinically identifiable white patches that may range from histologically-defined hyperkeratosis, dysplasia, carcinoma-in situ (CIS), or invasive SCC; in the hamster model they are commonly dysplasia, a precancerous condition [25]. Samples were imaged (*in vitro*) and signal intensity versus incident power was then characterized and

#140464 - $15.00 USD Received 4 Jan 2011; revised 8 Apr 2011; accepted 11 Apr 2011; published 13 Apr 2011

averaged for 3 animals (2-3 areas evaluated per lesion) at a consistent depth of 60 μm. Identical procedures were followed for unlabeled oral samples at the same imaging depth. The presence of GNRs in lesions was validated by 1) confirming low powers could be used to induce emission (0.2-0.7 mW as in the cell studies), 2) confirming the nonlinear nature of emission signal by observing the loss of signal with removal of laser modelock, and 3) qualitative characterization of excitation spectral response by loss of signal as laser was tuned away from the 780 nm absorption peak.

2.5. In vivo imaging

Hamsters were anesthetized and the buccal pouch secured to a sample holder for imaging as described above. *In vivo* imaging was performing on 5 DMBA hamsters and 2 untreated of comparable age. In this case visually identified lesion sites in DMBA hamsters and normal sites in control hamsters were imaged *in vivo* prior to i.v. delivery of GNRs as described above, at 10 minutes, and 24 hours with z-stacks obtained up to a depth of 230 microns. Sites of interest were located using a 10x 0.3 N.A. objective and images were collected using the 40x objective. A single confocal image was obtained of the imaged sites prior to the acquisition of a two photon z-stack. Biopsies were obtained at 24 hours and samples were immersed in formalin for fixation for 24 hours, then embedded in paraffin, sectioned, and stained with hematoxylin and eosin (H&E) for histological examination by a board certified pathologist (SQ).

To quantify vessel features, reconstructed 3D TPL images of the vascular network of dysplastic and normal sites were evaluated for 1) number of vessel branch junctions and 2) distance between branch junctions (vessel segment length). This was performed in a blinded manner with graders unaware of the pathological state of the imaged site. To measure distance between branch junctions, all vessel segments connecting two branch points/junctions were visually identified, then a line tool was manually drawn along the length of each segment to measure the distance of each segment in microns, keeping the line in the center of the vessel. Curved lines were used to capture the segment length of those vessels that were curved. The average line segment length was then calculated for each sampled site and an average taken per group (normal vs. dysplastic lesions). Quantification of vessel branch junction numbers was completed by manually counting all identified branch junctions per imaged sample and determining the average value for each group. Two of the image reconstructions were not of high enough quality to quantitatively measure morphometric features (although visually the increased vessel density and tortuous nature was evident) and were not included in the quantitative analysis. A Verhoeff-Van Gieson (VVG) stain was used to confirm presence of vessels within H&E sections. For each biopsy, a vessel count was performed on VVG stained single sections at 40x magnification

3. Results and discussion

Figure 1 presents typical two-photon images of labeled and unlabeled cells excited with 780 nm. Cells that had been incubated with GNRs typically had signals distributed throughout the cytoplasm, with nuclei appearing as dark regions, such as in the central dark regions of cells shown in the maximum intensity projection image of Fig. 1a, shown from a viewpoint of 0 degrees. Presence of GNR signal in the cytoplasm and periphery can be visualized in Fig. 1b, where cells were labeled with GNRs and subsequently with 5 μM Calcein-AM, a live cell stain. Cells were imaged using 0.4 mW for isolating GNR signal then at high power (8 mW) to capture Calcein-AM fluorescence. Single planes (xy, xz, yx) taken through the center of the larger cell demonstrate the localization of GNR signal within the cell as well as near the periphery. Figures 1d and e show overlays of TPL channel with transmitted light images of cells labeled (1d) and unlabeled (1e) with GNRs. Samples labeled with GNRs were illuminated with incident powers as low as 0.2 mW, which resulted in an average signal-to-

#140464 - $15.00 USD Received 4 Jan 2011; revised 8 Apr 2011; accepted 11 Apr 2011; published 13 Apr 2011

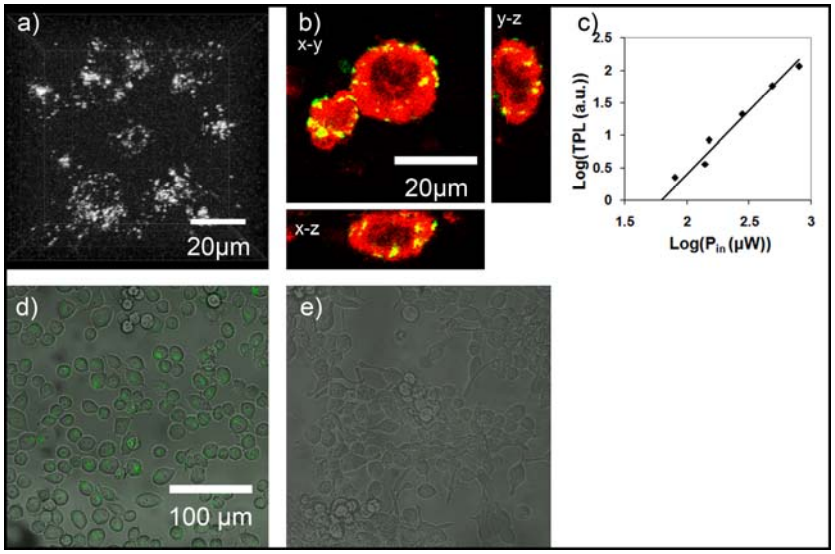

Fig. 1. Two-photon induced luminescence images of GNR-labeled and unlabeled JHU-19 oral squamous cell carcinoma cells. (a) Two-photon maximum intensity projection image of GNR-labeled cells using an incident power of 0.7 mW (image has been cropped to a dimension of ~50 by 50 microns to show details of cells). GNRs are distributed throughout cytoplasm, with nuclei appearing dark; (b) image of GNR labeled cell subsequently labeled with the live cell dye Calcein-AM, shown in red. Three planes through the midline of the cell are shown along three-dimensions (x-y, x-z,y-z) . (c) Graph demonstrating quadratic dependence of emission signal intensity on incident laser power. Slope of fitted line is 1.96; **(**d) Two-photon image of GNR-labeled cells using an incident power of 0.7 mW overlayed with corresponding transmitted light micrograph (e) Two-photon overlay image of unlabeled cells also using an incident power of 0.7 mW with detector and optical path settings unchanged.. Imaging was performed using a 40x 0.8 N.A. water immersion objective.

background ratio of 9.5, thus easily detected. Using an incident power of 0.7 mW, as in the case exhibited in Fig. 1d, resulted in a signal-to-background ratio of 24.9. No detectable signal was observed using equivalent incident laser powers on control (unlabeled) cells, as shown in Fig. 1e. Keeping all other conditions the same, incident laser powers greater than 35 mW were necessary to acquire similar signal-to-background values from native autofluorescence in unlabeled cells. Taking the laser out of mode-lock while illuminating the sample with the same incident power resulted in the disappearance of the signal from GNR labeled cells – confirming the detected signal to be nonlinear in nature. As shown in Fig. 1c, the TPL intensity (arbitrary units) was characterized as a function of power incident on the sample to confirm the quadratic dependence expected from a TPL response. A linear fit on the log-log plot of the data resulted in a slope of 1.96, confirming the expected quadratic dependence. Finally, microspectroscopy performed on the nanorods resulted in similar emission spectra to published results (shown in Fig. 3e) [3,4]. Thus, in these initial studies we confirmed the basic TPL characteristics of the GNRs and demonstrated their brightness in cells before implementing *in vivo* delivery.

In order to evaluate the potential benefits of GNRs for *in vivo* imaging, we performed tests to compare the luminescence signal from GNRs to that from native fluorophores in *ex vivo* oral mucosa tissue. Figure 2 shows the TPL response as a function of incident power for both autofluorescence and GNRs. This plot demonstrates significantly lower incident powers are required to excite GNRs than native fluorophores in order to obtain equivalent emission signals. Additionally, the quadratic dependence of the emission signal on incident power level was confirmed in both cases through a linear fit of the log-log plot, which had slopes of approximately 2; thus the signal detected was a two-photon signal. The expected signal difference between GNR TPL and AF TPL was found by determining the difference between

#140464 - $15.00 USD Received 4 Jan 2011; revised 8 Apr 2011; accepted 11 Apr 2011; published 13 Apr 2011

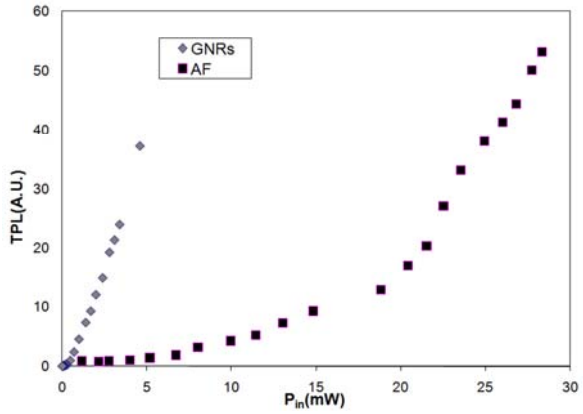

Fig. 2. Average trends displaying emission signal intensity vs. incident laser power for cases of gold nanorods and autofluorescence. In both cases, the quadratic dependency of two-photon emission signal on incident laser power was confirmed (the slope of a fitted line to log-log plots was ~2 for each case).

intercepts of the two log plots, resulting in a factor of 44 for this case. This value is reasonable given other studies have reported GNRs to be 50-60 times brighter than traditional fluorophores or native fluorophores in cells [3,4]. Since native autofluorescence can contribute substantial optical background signals when imaging with exogenous fluorophores, the absence of native autofluorescence at incident power levels where GNRs can be detected would benefit tissue imaging studies by reducing background signals that could affect interpretation of images. Another advantage in the use of GNRs is the desire to minimize the average powers incident on tissue. Thus, these *ex vivo* imaging studies in oral mucosa tissue with high autofluorescence and tissue having GNRs helped established the benefits of these contrast agents for allowing imaging in depth without confounding background autofluorescence while using low incident powers.

In vivo imaging: The results of *in vivo* imaging of non-targeted GNRs within the microvasculature of the normal hamster buccal pouch are demonstrated in Fig. 3. Confocal reflectance and multiphoton autofluorescence micrographs were taken prior to *in vivo* intravenous delivery of the GNRs; in both cases, blood vessels appear dark compared to surrounding tissue (Figs. 3a and 3b). It is worth noting that an incident power of 20 mW was needed to obtain the multiphoton autofluorescence micrograph displayed, and it was confirmed that up to this high incident power, no emission signal was detected from the vessels. In contrast, the image shown in Fig. 3c was obtained following intravenous injection of the GNRs using an incident power of 1 mW at a depth starting at 60 μm (to 175 μm) at the same vessel site shown in Figs. 3a and 3b. As can be seen in Fig. 3c, using GNRs as a contrast agent, microvasculature in this normal site can easily be visualized using low incident powers that are sub-threshold for obtaining background autofluorescence.

The spectral profile shown in Fig. 3d for the *ex vivo* GNRs was similar to those that have been previously reported in the literature in *ex vivo* experiments [3,4]. As shown in Fig. 3d, the *in vivo* and *ex vivo* spectra are identical except for slight differences in the 400-450 nm range. These differences are attributed to reabsorption and scattering of this lower wavelength light in tissue, such as reabsorption by hemoglobin. Thus, despite this slight difference, the *in vivo* microenvironment did not significantly alter the spectral properties of the GNRs.

#140464 - $15.00 USD Received 4 Jan 2011; revised 8 Apr 2011; accepted 11 Apr 2011; published 13 Apr 2011

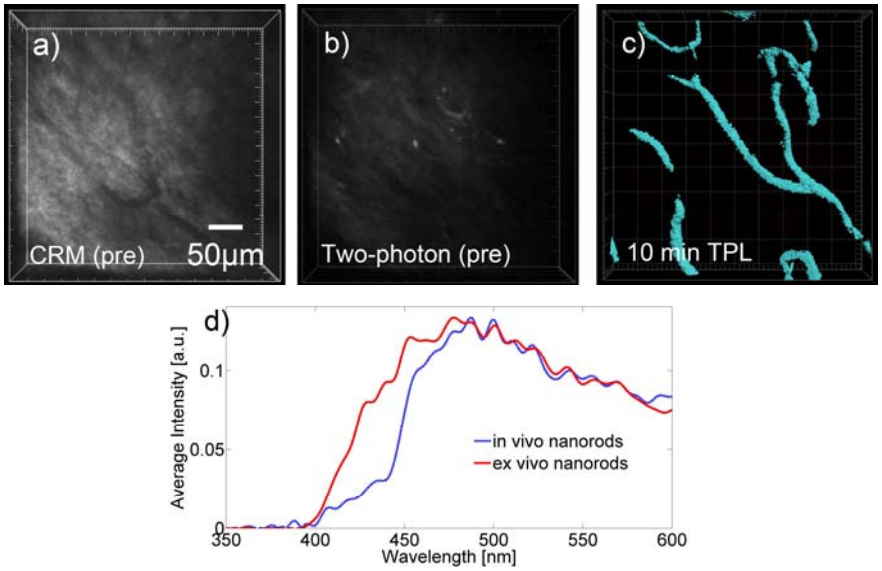

Fig. 3. Representative two-photon microscopy images of intravenously delivered GNRs in hamster model with accompanying confocal reflectance image (a) Confocal reflectance image of tissue showing location of blood vessels which appear dark against the surrounding tissue (b) High power (20 mW) two photon image of the same vascular region prior to intravenous injection of GNRs (c) Two-photon image using low incident power of 1 mW following intravenous injection GNRs showing blood vessels in the tissue. Two-photon microscopy of vascular sites prior to GNR injection, using 1-20 mW incident power, yielded no detectable signal from blood vessels. Asterisk denotes the same vessel junction on all three images displayed. (d) Spectral profile of GNRs *in vitro* and within *in vivo* blood vessels following intravenous injection.

Intravenous injection of GNRs into DMBA-treated animals allowed for the abnormal vascular structure of the dysplastic mucosa to be visualized using low incident powers ranging from 0.2 mW to 1 mW, and up to 230 microns in depth without the presence of confounding autofluorescence. The microvasculature of DMBA-transformed mucosa at 10 minutes appeared highly dense and tortuous with more branching points than those of normal oral mucosa such as the case in Fig. 3c (Fig. 4a).

Two-photon image of lesion 24 hours post-inoculation using same incident power of 1 mW. In this case GNRs are distributed throughout the volume of the imaged lesion, rather than confined to the vascular space (c) Confocal reflectance image acquired at 10x magnification used to microscopically identify lesion surface prior to two-photon microscopy. Asterisk denotes image artifact. (d) Histology of lesion, stained with VVG stain. Some identified vessels are located at sites of the asterisks (*).

Interestingly, blood vessel counts in stained histology sections revealed significantly more vessels in single sections from dysplastic sites than normal sites, as indicated in Table 1. Analyzed TPL images revealed that dysplastic sites had an increased number of vessel junctions and were highly tortuous (decreased distance between vessel branch junctions). Histology slides provide a single slice view of a tissue site, whereas 3D volumes are provided in TPL. While a direct comparison of vessel numbers between histology sections and 3D TPL is challenging and beyond the scope of the current study, in TPL the increased density of vessels, the decreased distance between vessel branch junctions, and increased number of vessel junctions provide a basis for why more vessels are seen in histology cross-sections.

Post-injection, GNRs were allowed to circulate for 24 hours and then sites were re-imaged with two-photon microscopy to visualize GNR distribution in the lesion sites at that time point, followed by biopsy. Typical results indicated a diffused pattern of GNR distribution,

#140464 - $15.00 USD Received 4 Jan 2011; revised 8 Apr 2011; accepted 11 Apr 2011; published 13 Apr 2011

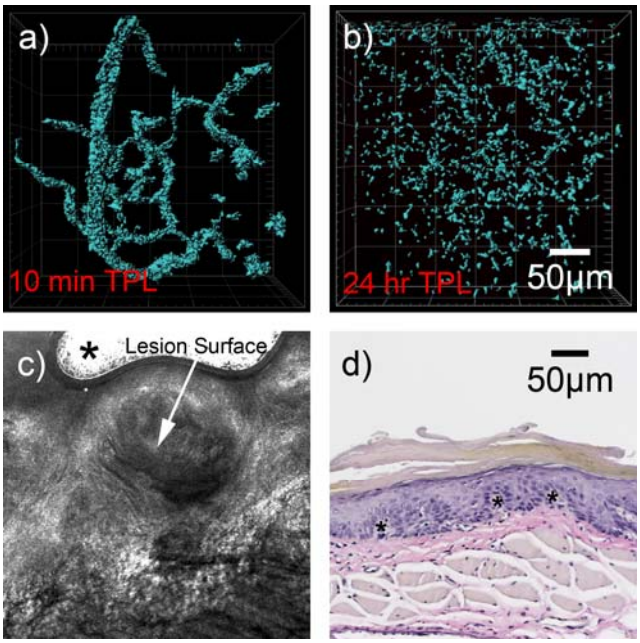

Fig. 4. (a) Two-photon 3D reconstructed image of precancerous (dysplastic) lesion labeled with GNRs 10 minutes post-inoculation, showing dense and tortuous network of blood vessels, obtained with an incident power of 1 mW. (b)

Table 1. Comparison of blood vessel features in histology and TPL[a]

	Histology Evaluation # of Vessels	TPL Image Parameters	
		Ave Vessel Segment Length	Vessel Junctions
Normal	0.8 ± 0.5	111 ± 19	6 ± 2
Dysplasia	8.3 ± 2.5	44 ± 10	16 ± 4

[a]Single VVG stained sections from lesions and control sites were assessed for number of blood vessels in the histology evaluation. In TPL, the number of vessel junctions and the distance between vessel branch junctions (vessel segment length) were obtained in imaged volumes. The decreased vessel segment length and increased number of vessel junctions in DMBA-treated (dysplastic) sites indicate measures of increased vessel density and abnormal structure and are consistent with the increased number of vessel counts in histology sections.

which did not appear to be confined within vessel sites, but rather distributed throughout the lesion area (Fig. 4b). GNRs were still clearly confined to the microvasculature. In contrast to dysplastic sites, the microvasculature of normal sites and control animals not treated with DMBA still had circulating GNRs after 24 hours. This observed difference between the apparent distributions of GNRs in dysplastic lesions as compared to normal oral tissue is possibly due to passage of the GNRs into the lesion space from the abnormal microvasculature, which would occur if the blood vessels were leaky. A hallmark of tumor angiogenesis is abnormal blood vessels which are leaky [26]. Interestingly, recent evidence of the presence of angiogenesis in dysplasia has been shown (including dysplasia of the oral mucosa) [27–29]. Thus, given these recent findings, it would be expected that vessels of dysplastic lesions be leaky compared to normal vessels. This feasibility study sets the stage for a broader *in vivo* angiogenesis imaging study using GNRs.

4. Conclusions

In this study, the feasibility of using GNRs as efficient contrast agents for *in vivo* imaging of features of oral carcinogenesis was evaluated following cellular and *in vitro* characterization of their properties. We found GNRs to be useful in visualizing the abnormal 3-dimensional

#140464 - $15.00 USD Received 4 Jan 2011; revised 8 Apr 2011; accepted 11 Apr 2011; published 13 Apr 2011

vascular structure present in dysplastic oral mucosa using much lower incident powers than those needed for autofluorescence and for typical fluorophores on our system. Images revealed dense and tortuous blood vessels with results consistent with histological features and recent studies that indicate angiogenesis in dysplasia. To our knowledge, this is the first time TPL of GNRs has been used to image *in vivo* features in a cancer model and also the first time the abnormal vasculature of precancerous lesions has been visualized by intravital microscopy. These initial results suggest that GNRs can function as high-contrast imaging agents for visualization of *in vivo* features of carcinogenesis, with potential applications to be explored in studies of carcinogenesis, development of therapeutic approaches providing real-time feedback of effects, and/or diagnostics. While the goal of the current study was to demonstrate advantages of nontargeted GNRs for *in vivo* cancer imaging, it will be of interest to pursue *in vivo* molecular targeting to specific biomarkers which could prove useful in early diagnostics or studies of pathogenesis in oral carcinogenesis.

Acknowledgments

Financial support from the National Institutes of Health, National Cancer Institute (R01 CA127429) and NSF (0933782) is gratefully acknowledged. We thank Adriana Paulucci and the Optical Microscopy Core at UTMB for use of Imaris 3-D visualization software. Special thanks to Dr. Vicente Resto, Interim Chair, Dept of Otolaryngology, for numerous helpful discussions regarding oral precancers and SCC and for the JHU-19 oral squamous cell carcinoma cell line. S. Motamedi and T. Shilagard contributed equally to this work.

#140464 - $15.00 USD Received 4 Jan 2011; revised 8 Apr 2011; accepted 11 Apr 2011; published 13 Apr 2011